# Chapter 3
# Monometallic Catalyst: Performance and Shape Morphology Effect

## 3.1 Monometallic Catalysts for steam methane reforming

Nickel (Ni)-based monometallic catalysts are widely utilized for steam methane reforming (SMR) due to their cost-effectiveness, high catalytic activity, and ability to dissociate methane efficiently. The performance of Ni catalysts is heavily influenced by the choice of support material, as the support not only disperses the active metal but also affects the catalyst's thermal stability, reducibility, and resistance to coking.

### 3.1.1 Nickel Catalysts on Alumina Support

Alumina ($Al_2O_3$) is one of the most commonly used support materials for nickel catalysts in steam methane reforming. [1-2] Its high surface area, thermal stability, and moderate acidity make it an excellent choice for anchoring nickel nanoparticles. Alumina-supported nickel catalysts are known for their ability to achieve high methane conversion rates at elevated temperatures (700–900°C). The interaction between nickel and alumina facilitates the dispersion of nickel particles, preventing agglomeration and maintaining catalytic activity over prolonged periods. [3]

However, alumina-supported Ni catalysts face challenges such as carbon deposition and sintering at high temperatures. [4] The acidic nature of alumina can promote coke formation through polymerization of hydrocarbons, leading to catalyst deactivation. To mitigate this, modifications like doping alumina with alkali or alkaline earth metals (e.g., Mg, Ca, or K) are employed to reduce acidity and enhance coke resistance. [5-7] These modifications also improve the basicity of the catalyst surface, which promotes the adsorption and activation

of water molecules, thereby aiding in the removal of surface carbon through the water-gas shift reaction.

### 3.1.2 Nickel Catalysts on Ceria Support

Ceria ($CeO_2$) has gained significant attention as a support material for Ni-based catalysts due to its unique redox properties and high oxygen storage capacity (OSC). Ceria can undergo reversible redox cycles ($Ce^{4+} \leftrightarrow Ce^{3+}$) under reaction conditions, which facilitates the formation and removal of oxygen vacancies. These oxygen vacancies play a crucial role in mitigating carbon deposition during steam methane reforming by enhancing the oxidative removal of surface carbon species. [8-10]

Nickel catalysts supported on ceria exhibit superior catalytic activity and stability compared to alumina-supported catalysts, particularly under low-temperature reforming conditions. Ceria's ability to promote strong metal-support interaction helps in stabilizing nickel particles, reducing sintering, and enhancing resistance to coking. [11-13] Furthermore, ceria supports enhance the water-gas shift (WGS) reaction, increasing hydrogen yield and reducing CO levels in the product stream. This makes $Ni/CeO_2$ catalysts particularly attractive for applications where hydrogen purity is critical.

*Challenges and Future Directions*

Despite their advantages, both alumina and ceria supported Ni catalysts have limitations. Alumina-based catalysts require surface modifications to counteract coking, while ceria-based catalysts often suffer from lower mechanical strength and higher costs. Future research is focusing on developing advanced preparation techniques, such as co-precipitation, sol-gel synthesis, and hydrothermal methods, to optimize the dispersion of nickel and improve the structural properties of the support. [14-15] Additionally, exploring doping strategies with rare earth elements or alkali metals can further enhance the

performance and durability of these catalysts in industrial-scale steam methane reforming processes.

In summary, nickel-based monometallic catalysts supported on alumina and ceria represent a balance between economic feasibility and catalytic performance for steam methane reforming. Their application in hydrogen production continues to evolve, with ongoing research addressing challenges related to stability, coking, and scalability.

### 3.1.3 Key literature review on Ni based monometallic catalyst

Below is a key literature table (Table 3.1) for nickel-based monometallic catalysts supported on alumina and ceria. This table summarizes key details often discussed in research studies:

**Table 3.1** Literature survey on Nickel based monometallic catalyst

| Catalyst | Support | Reaction conditions | Performance | Key findings | References |
|---|---|---|---|---|---|
| $Ni/CeO_2$ | Ceria | Steam reforming of methane 600°C, 1 atm, $H_2O:CH_4$ = stoichiometric | Effective and stable methane reforming | $Ni/CeO_2$ catalysts doped with La, Pr, or Zr showed stability and effectiveness at mild conditions. | Iglesias et al., 2017[16] |
| $Ni/Al_2O_4$ | Alumina | Steam reforming of methane 748–823 K, 120 kPa, $H_2O:CH_4$ = 4:1 | Catalyst deactivation observed with time | Catalyst activity decreases over time, influenced by particle size and hydrogen:methane ratio | Hou& Hughes, 2001[17] |

| | | | | | |
|---|---|---|---|---|---|
| $Ni/CeO_2$ | Ceria | Steam reforming of methane 700°C, 1 atm, $H_2O:CH_4$=4:1 | $CH_4$ conversion: 70% (nanocube calcined at 550°C) | Impact of ceria morphology on hydrogen production in methane steam reforming for membrane reformers. | Baudh et al., 2024 [18] |
| $Ni/Al_2O_3$ | Alumina | 750°C, 1 atm, $H_2O:CH_4$=3:1 | $CH_4$ conversion: 89%; $H_2$ yield: 80% | Alumina-based catalysts show cost-effectiveness but require higher Ni loading. | Patel et al., 2020 [19] |
| $Ni/CeO_2$ | Ceria | Steam reforming of glycerol; typically, 500–600°C | High hydrogen yield and glycerol conversion. | The $Ni/CeO_2$ catalyst prepared by the precipitation deposition method offers high activity for glycerol reforming, with efficient hydrogen production. | Pant et al., 2011 [20] |
| Cu-promoted Ni | $SiO_2$ | Methane decomposition (thermocatalytic); typically, 600–700°C | High $H_2$ yield and carbon nanotube formation. | Copper promotion significantly enhances the catalyst's performance for both hydrogen production and carbon nanotube synthesis. | Saraswat et al., 2013 [21] |

| | | | | | |
|---|---|---|---|---|---|
| Ni | Alumina | Steam reforming of methane; typically 700–900°C | High methane conversion and stable $H_2$ production. | The study investigates the reaction mechanism of methane steam reforming over $Ni/Al_2O_3$ catalysts, with Ni and $Al_2O_3$ playing key roles in the reaction process. Insights into catalyst deactivation are also provided. | Ross et al., 1973 [22] |
| Ni | Ceria | Steam reforming of methane; typically 700–900°C, 1:1 ($H_2O/CH_4$) ratio | Coke-free methane steam reforming with high methane conversion. | The study investigates the active sites and reaction pathway for coke-free methane steam reforming on a $Ni/CeO_2$ catalyst. Metal–support interactions are critical for preventing coke formation and enhancing the stability of the catalyst. | Salcedo et al., 2021 [23] |

| | | | | | |
|---|---|---|---|---|---|
| Ni-based | $Al_2O_3$, $CeO_2$ | Methane tri-reforming with industrial flue gas; typically, 700–850°C, 1:1:1 ($H_2/CO_2/N_2$) ratio | Improved methane conversion and flue gas utilization. | The study focuses on optimizing the metal-support interaction in methane tri-reforming catalysts, showing that tuning these interactions enhances performance for industrial flue gas utilization. | Kumar et al., 2020 [24] |

### 3.2 Preparation of monometallic catalysts

Ni based monometallic catalyst is synthesized using wet impregnation method on both alumina and ceria supports. Commercial alumina and ceria are used for the study. As we have seen commercial ceria is showing high catalytic activity as compared to nanorod and nanocube shapes. Therefore, commercial ceria is used for the further study. Nickel nitrate hexahydrate, aluminium oxide and cerium oxide salts were used for the synthesis of monometallic catalyst. After mixing the solution, pH is maintained at 7 and temperature kept constant at 70℃. The solution is left for continuous stirring for atleast 3 hours. The catalyst slurry obtained kept in oven at temperature 120℃ for overnight. The dried catalyst is then calcined in muffle furnace at 970℃ for 5-6 hours. Final monometallic catalyst is obtained and used for the testing for steam methane reforming as shown in Fig 3.1.

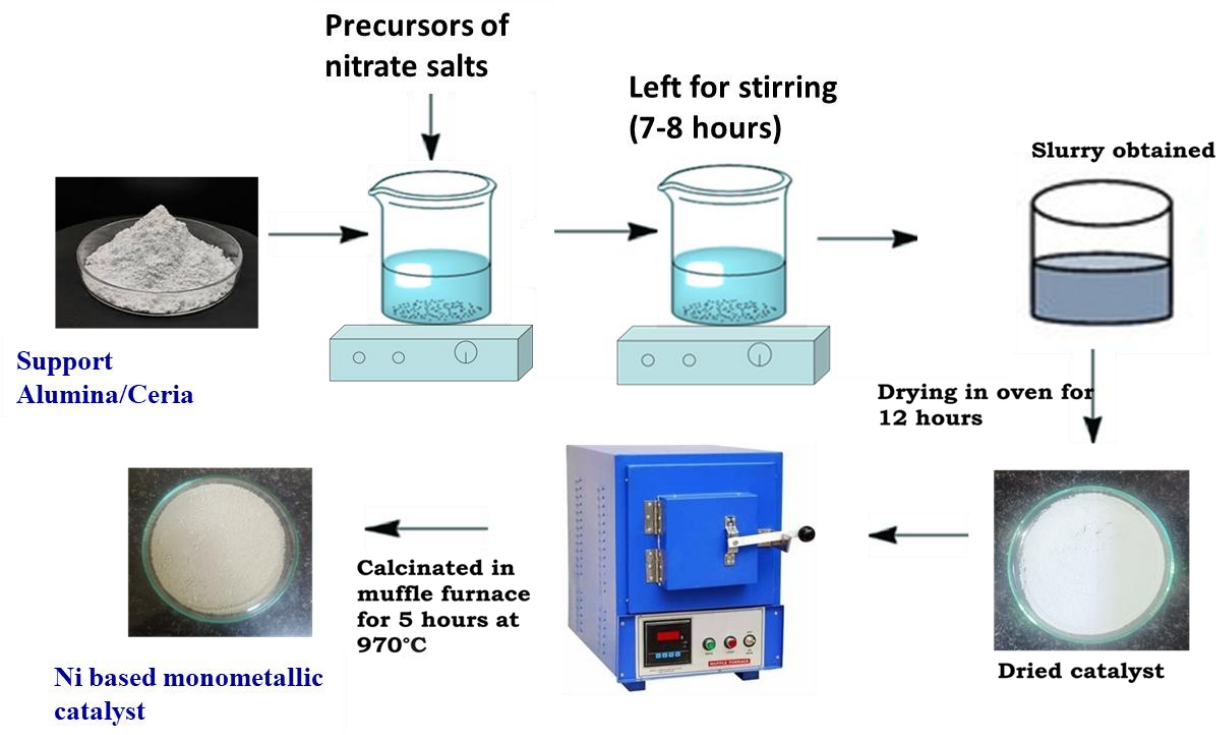


**Fig. 3.1** Wet impregnation method for monometallic catalysts

## 3.3 Results and discussion

### 3.3.1 SEM

The SEM images depict the surface morphology of various catalysts synthesized for steam methane reforming, comparing metal catalysts supported on $CeO_2$ (ceria) and $Al_2O_3$ (alumina) as shown in Fig 3.2. In the first row, Ni/$CeO_2$, La/$CeO_2$, Co/$CeO_2$, and Fe/$CeO_2$ are shown. Ni/$CeO_2$ exhibits a porous structure with well-dispersed particles, which facilitates enhanced catalytic activity and stability by providing better metal-support interaction and high oxygen mobility. [25] La/$CeO_2$ shows a rough, uneven morphology, likely reflecting La role in enhancing the redox properties of ceria. Co/$CeO_2$ and Fe/$CeO_2$ display relatively denser surfaces, with Fe/$CeO_2$ appearing particularly compact and smooth, potentially contributing to lower catalytic activity due to reduced surface area and accessibility for reactants. [25]

The second row shows Ni, La, Co, and Fe catalysts supported on $Al_2O_3$. Ni/$Al_2O_3$ has a

less porous structure compared to $Ni/CeO_2$, which may limit its redox capability but still provides good activity due to the thermal stability of alumina. $La/Al_2O_3$ and $Co/Al_2O_3$ display grainy and aggregated particles, which could impact the dispersion of the active metal and reduce performance. $Fe/Al_2O_3$ shows a similarly compact morphology as $Fe/CeO_2$, which may further explain its lower catalytic performance. Overall, the images suggest that ceria-supported catalysts, particularly $Ni/CeO_2$, are better suited for steam methane reforming due to their superior textural and redox properties, while alumina-supported catalysts are more thermally stable but may be less active.

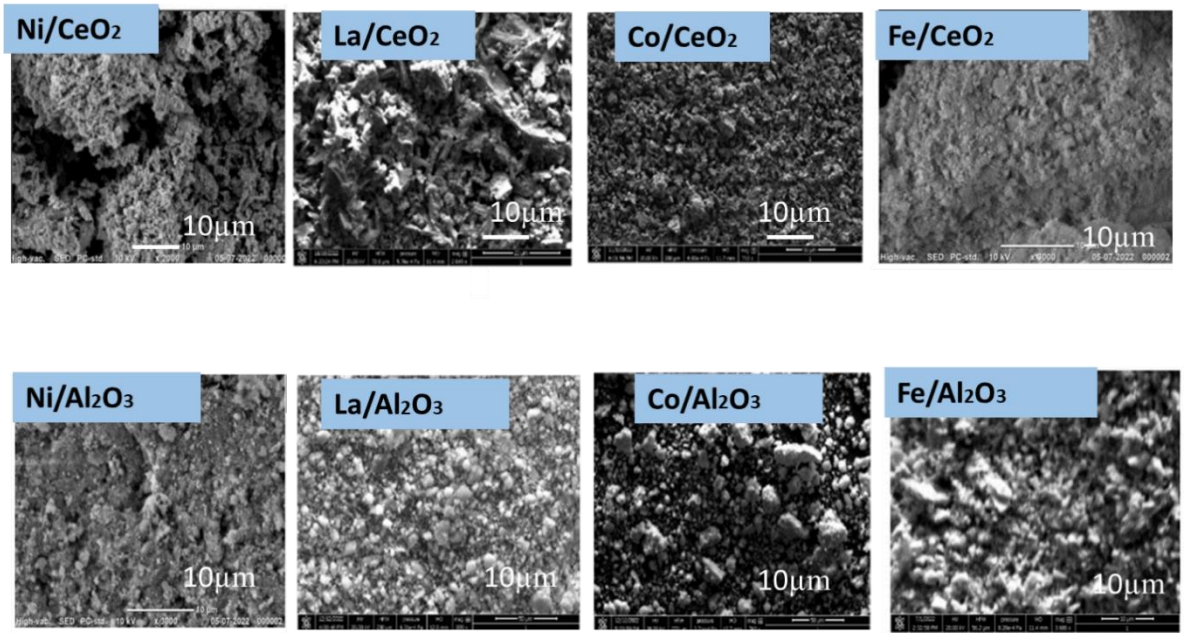


**Fig. 3.2** SEM images of monometallic ceria and alumina supported catalysts

### 3.3.2 XRD

The XRD patterns illustrate the crystalline phases present in various catalysts synthesized for steam methane reforming, focusing on metal oxides supported on ceria ($CeO_2$) and alumina ($Al_2O_3$). The peaks corresponding to $CeO_2$ are prominently observed in the catalysts supported on ceria, as indicated by sharp reflections associated with its fluorite structure. These peaks confirm the high crystallinity of ceria, which contributes to its

excellent oxygen storage capacity and redox properties, crucial for catalytic performance in steam methane reforming.

For $Ni/CeO_2$, additional peaks for NiO are observed, indicating the presence of nickel oxide, which serves as the active phase in reforming reactions. In $Co/CeO_2$, CoO peaks are evident, while $La/CeO_2$ and $Fe/CeO_2$ show reflections corresponding to $La_2O_3$ and FeO, respectively. These metal oxides influence the catalytic activity and redox behavior of the catalysts, with NiO generally demonstrating superior performance for methane reforming. (Fig 3.3)

The alumina-supported catalysts exhibit characteristic reflections for $\gamma$-$Al_2O_3$, indicative of its high surface area and thermal stability. Peaks for NiO, CoO, $La_2O_3$, and FeO are also visible in their respective catalysts, confirming the successful incorporation of the metal oxides. However, the peaks for the active phases appear broader for alumina-supported catalysts, suggesting smaller crystallite sizes or better dispersion compared to ceria-supported counterparts.

Overall, the XRD patterns highlight the structural differences between ceria- and alumina-supported catalysts, with ceria providing additional redox functionality through its oxygen storage and release capabilities, which is especially beneficial for steam methane reforming.[26] Nickel-based catalysts exhibit the most pronounced reflections for active phases, aligning with their established high catalytic activity in reforming reactions.

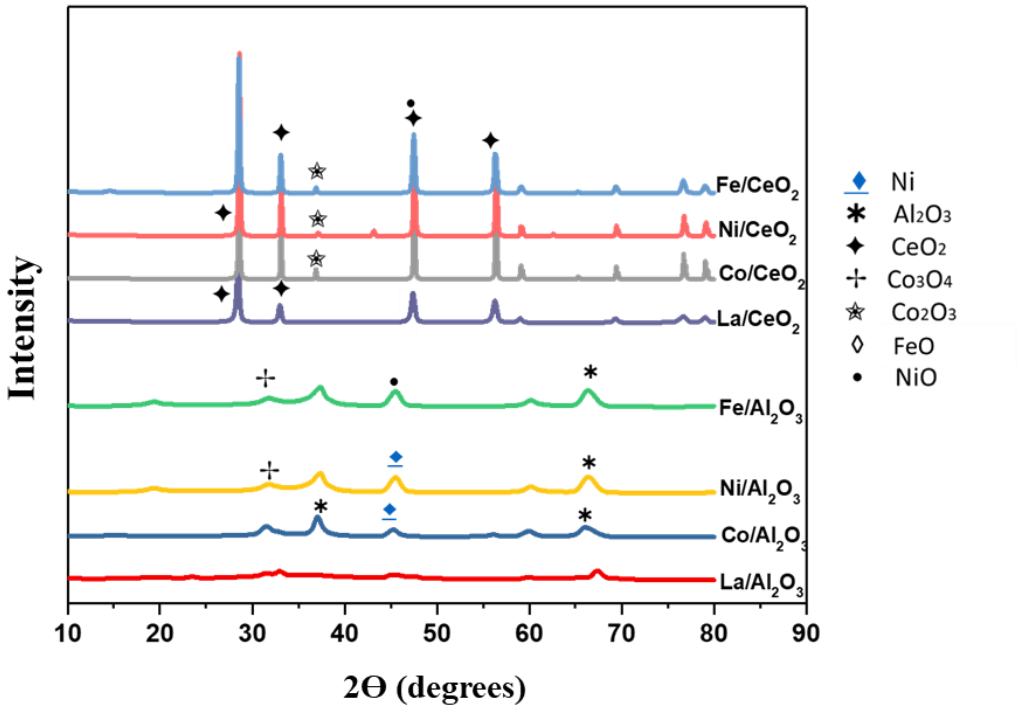


**Fig. 3.3** XRD graph of monometallic catalysts

### 3.3.3 BET

The BET surface area analysis presented in the graph illustrates the nitrogen adsorption-desorption isotherms for different catalysts synthesized for steam methane reforming. The isotherms exhibit a characteristic shape indicative of mesoporous materials, which are favorable for catalytic applications due to their high surface area and enhanced reactant accessibility. Fig 3.4 represents the BET isotherms of alumina and ceria supported monometallic catalysts.

Among the catalysts, $Ni/CeO_2$ shows the highest adsorption capacity, reflecting its large surface area and well-developed porous structure, which are crucial for effective catalytic performance. This enhanced surface area facilitates better dispersion of the active nickel species and improves the availability of active sites for methane conversion. $Co/CeO_2$ and $La/CeO_2$ demonstrate intermediate adsorption behavior, suggesting a relatively smaller

surface area or less developed porosity compared to $Ni/CeO_2$. $Fe/CeO_2$ displays the lowest adsorption capacity, indicating a less porous structure, which may contribute to its reduced catalytic performance in steam methane reforming.

The alumina-supported catalysts exhibit a similar trend, with $Ni/Al_2O_3$ showing higher adsorption than its counterparts. However, the overall adsorption capacity is lower for $Al_2O_3$-supported catalysts compared to $CeO_2$-supported ones, reflecting the difference in textural and redox properties between the supports. The $CeO_2$ supported catalysts generally benefit from their oxygen storage capacity and better interaction with the active metals, which enhances the catalytic activity and stability for steam methane reforming. Overall, the BET analysis underscores the importance of high surface area and well-developed porosity for efficient catalyst performance, with $Ni/CeO_2$ emerging as the most promising candidate for steam methane reforming due to its superior textural properties.

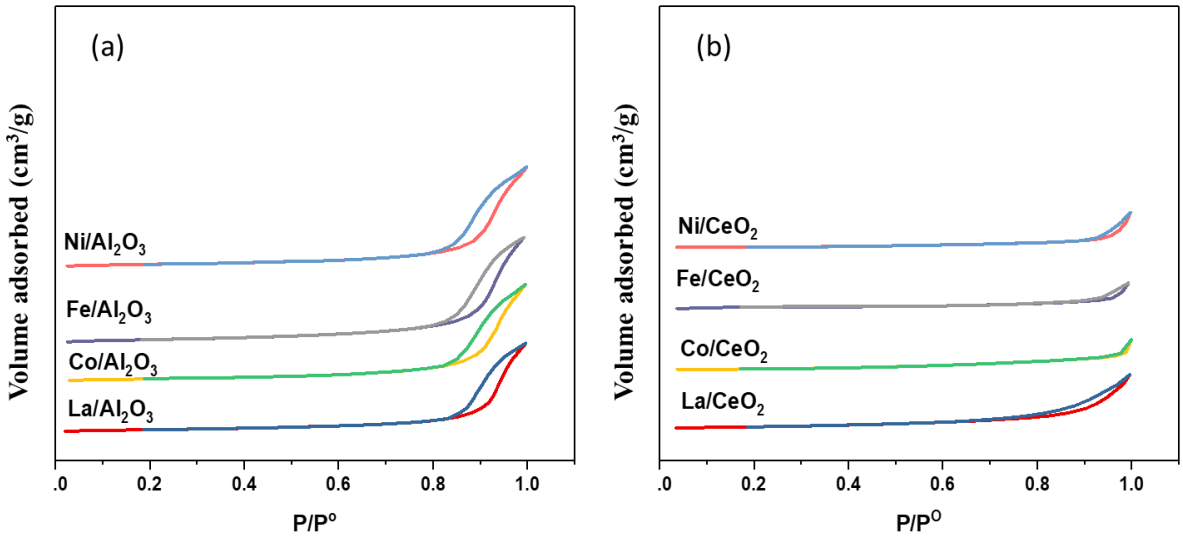


**Fig. 3.4** BET graphs of monometallic catalysts (a) alumina supported (b) ceria supported

The Table 3.2 summarizes the textural and structural properties of different catalysts synthesized for steam methane reforming. Key properties, including surface area, pore

volume, pore diameter, crystallite size, and the type of isotherm, vary significantly depending on the metal and support used.

$Al_2O_3$ supported catalysts (Ni/ $Al_2O_3$, Co/ $Al_2O_3$, La/ $Al_2O_3$, Fe/ $Al_2O_3$) exhibit relatively high surface areas (78–106 $m^2/g$) and pore volumes (0.34–0.39 $cm^3/g$), with moderate pore diameters (6.3–28.1 nm). The crystallite sizes range from 7.2 nm ($Fe/Al_2O_3$) to 13.3 nm (Ni/ $Al_2O_3$). All these catalysts display **Type IV isotherms**, indicative of mesoporous structures suitable for gas-phase reactions. The high surface area and mesoporosity enhance the dispersion of active metal species, contributing to catalytic performance. $CeO_2$ supported catalysts ($Ni/CeO_2$, $Co/CeO_2$, $La/CeO_2$, $Fe/CeO_2$) show significantly lower surface areas (5–12 $m^2/g$) and pore volumes (0.009–0.036 $cm^3/g$), with varying pore diameters (6.7–23.6 nm). Crystallite sizes are generally larger, particularly for $Co/CeO_2$ (64.07 nm). These catalysts exhibit **Type II isotherms**, suggesting the presence of non-porous or macroporous structures. Despite lower surface area, ceria provides strong metal-support interactions and oxygen storage capacity, which are critical for steam methane reforming.

Overall, Ni-based catalysts show promising properties due to their moderate surface area and optimal crystallite size, particularly when supported on $Al_2O_3$. [27-28] $CeO_2$ supported catalysts may be advantageous for their redox properties despite their lower textural properties. [29-31]

**Table 3.2** Surface area, pore volume, pore diameter and crystallite size for monometallic alumina supported catalysts

| Catalyst | Surface Area ($m^2/g$) | Pore Volume ($cm^3/g$) | Pore Diameter (nm) | Crystallite size (nm) | Type of isotherm |
|---|---|---|---|---|---|
| **$Ni/Al_2O_3$** | 106.034 | 0.384 | 6.296 | 13.375 | Type 4 |
| **$Co/Al_2O_3$** | 86.684 | 0.394 | 28.135 | 9.153 | Type 4 |
| **$La/Al_2O_3$** | 78.845 | 0.343 | 27.780 | 10.124 | Type 4 |
| **$Fe/Al_2O_3$** | 96.457 | 0.344 | 8.822 | 7.234 | Type 4 |
| **$Ni/CeO_2$** | 12.324 | 0.030 | 6.773 | 24.542 | Type 2 |
| **$La/CeO_2$** | 11.133 | 0.036 | 23.601 | 25.451 | Type 2 |
| **$Co/CeO_2$** | 6.301 | 0.025 | 15.603 | 64.071 | Type 2 |
| **$Fe/CeO_2$** | 5.343 | 0.009 | 8.627 | 25.242 | Type 2 |

### 3.3.4 Activity Results

The graph compares the catalytic performance of four catalysts Ni/ $Al_2O_3$, Co/ $Al_2O_3$, La/ $Al_2O_3$, and Fe/ $Al_2O_3$ over time, showing their activity in terms of conversion percentage as shown in Fig 3.5. Ni/ $Al_2O_3$ demonstrates exceptional stability, maintaining nearly constant activity throughout the duration of the experiment, indicating its superior resistance to deactivation. In contrast, Co/ $Al_2O_3$ starts with moderate activity but experiences a rapid decline, stabilizing at a significantly lower level.[32] Similarly, La/ $Al_2O_3$ begins with higher activity than Co/ $Al_2O_3$ but exhibits a sharp drop before leveling off at an intermediate value. Fe/ $Al_2O_3$, which starts at a comparable activity to La/ $Al_2O_3$, shows the steepest decline, eventually stabilizing at the lowest activity among the catalysts. These trends suggest that Ni/ $Al_2O_3$ is the most durable catalyst, likely due to better structural stability, resistance to sintering, or reduced susceptibility to poisoning. The other catalysts decline could be attributed to structural changes, active site oxidation, or carbon

deposition. These findings highlight the importance of catalyst selection for maintaining long-term performance in catalytic processes.

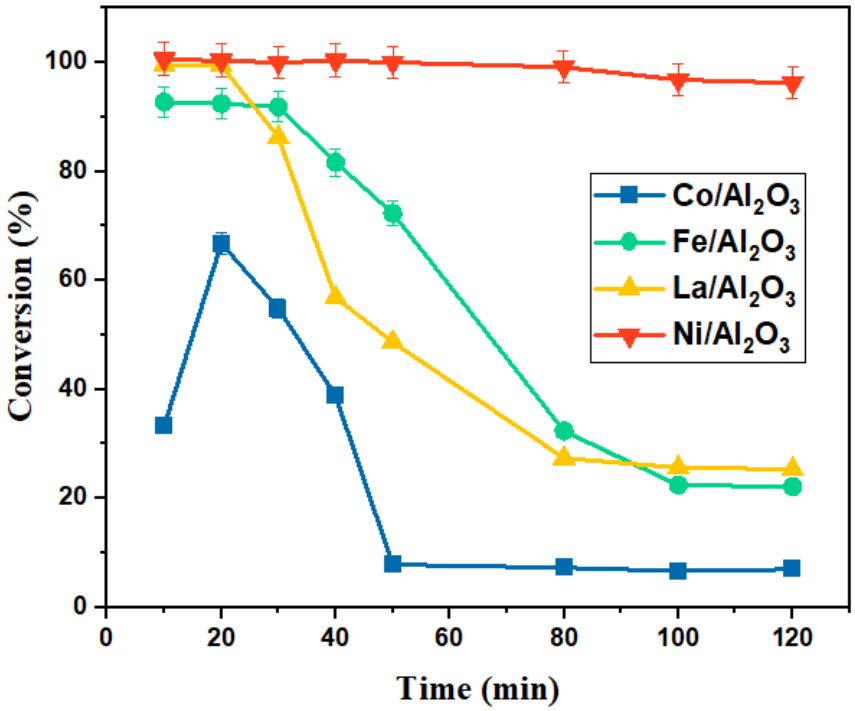


**Fig. 3.5** Conversion vs time graph of monometallic alumina supported catalysts

Fig 3.6 illustrates the catalytic activity of $Ni/CeO_2$, $Co/CeO_2$, $La/CeO_2$, and $Fe/CeO_2$ catalysts over time. Among these, $Ni/CeO_2$ exhibits a significant increase in activity initially, surpassing all other catalysts, and continues to improve slightly over time, indicating strong catalytic performance and stability. $La/CeO_2$ also shows a notable rise in activity early on, stabilizing at a high level, though slightly below that of $Ni/CeO_2$.[33] $Co/CeO_2$ initially achieves the highest activity at the start but then declines steadily and stabilizes at a much lower activity. $Fe/CeO_2$ shows the least favorable performance, with a sharp initial increase followed by a steep decline, ultimately stabilizing at the lowest activity.

The trends suggest that $Ni/CeO_2$ is the most effective and stable catalyst, likely due to its superior resistance to deactivation mechanisms such as sintering or coking. $La/CeO_2$ also demonstrates good catalytic performance, potentially benefiting from its interaction with the $CeO_2$ support. In contrast, the decline in $Co/CeO_2$ and $Fe/CeO_2$ could be attributed to rapid structural degradation or poisoning of active sites. These findings highlight the importance of both the active metal and the $CeO_2$ support in achieving high and sustained catalytic activity.

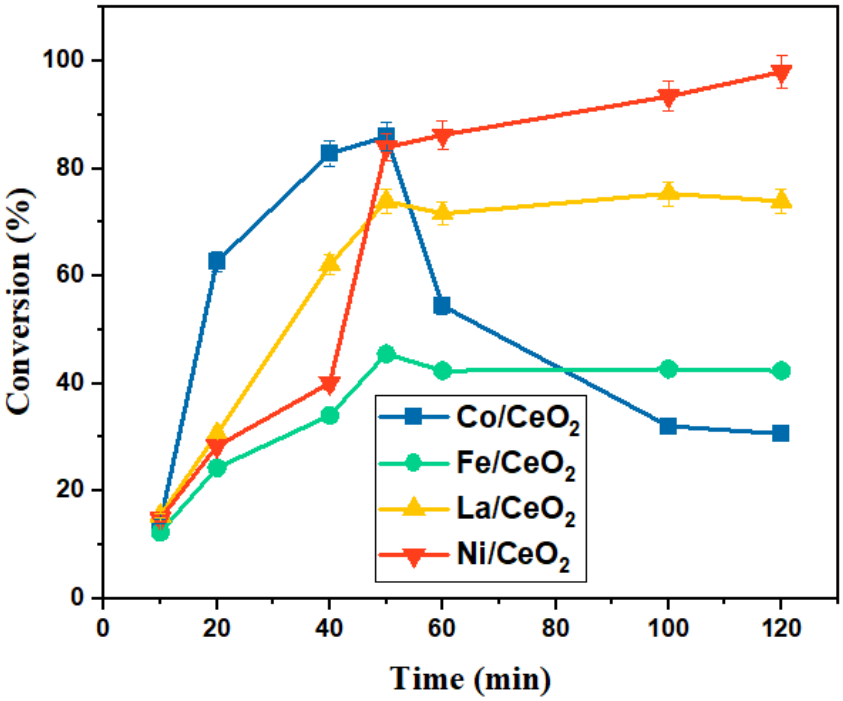


**Fig. 3.6** Conversion vs time graph of monometallic ceria supported catalysts

This graph presents the catalytic performance of $Ni/Al_2O_3$, $Co/Al_2O_3$, $La/Al_2O_3$, and $Fe/Al_2O_3$ for steam methane reforming (SMR) over time. $Ni/Al_2O_3$ shows consistently high and stable activity throughout the reaction, highlighting its effectiveness and durability as a catalyst for SMR. In comparison, $Co/Al_2O_3$ maintains a moderate level of activity, which remains relatively stable over time. Both $La/Al_2O_3$ and $Fe/Al_2O_3$ demonstrate significantly

lower initial activity, with $La/Al_2O_3$ showing a slight decline and $Fe/Al_2O_3$ stabilizing at the lowest activity among the four catalysts.

The superior performance of $Ni/Al_2O_3$ can be attributed to the high activity of nickel in activating methane and its strong interaction with the $Al_2O_3$ support, which provides thermal stability and resistance to sintering. $Co/Al_2O_3$ exhibits moderate activity, likely due to cobalt's ability to catalyze SMR, though less efficiently than nickel.[34] The poor performance of $La/Al_2O_3$ and $Fe/Al_2O_3$ may stem from lower intrinsic activity of lanthanum and iron for methane activation and possible deactivation mechanisms, such as carbon deposition or oxidation. Overall, $Ni/Al_2O_3$ emerges as the most promising catalyst for sustained SMR applications. CO selectivity of $Ni/Al_2O_3$ is high as compared to other catalysts but conversion is also high for this catalyst as compared to others. Therefore, choice of Ni based bimetallic catalyst with promoters La, Fe and Co with both alumina and ceria supports to get maximum conversion with CO selectivity. [35] As per our objective of membrane reformer and fuel cell, CO content should be minimized.

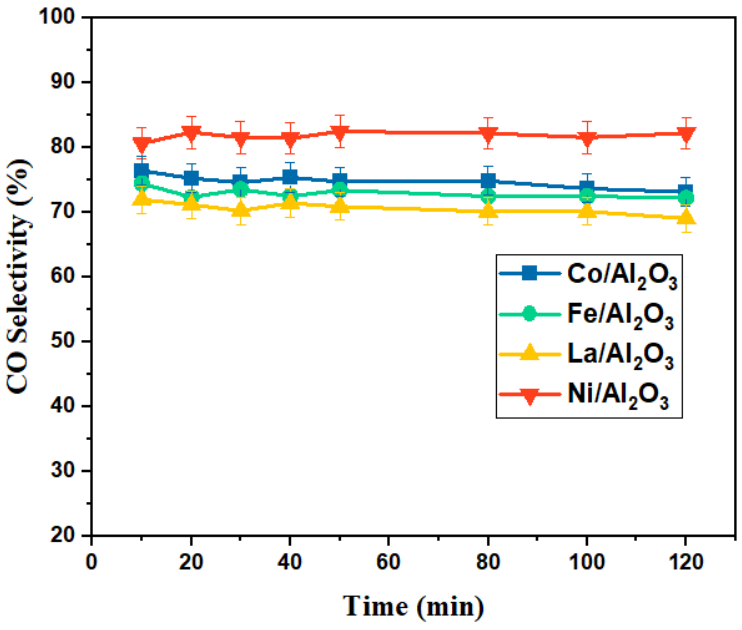


**Fig. 3.7** CO selectivity vs time of monometallic alumina supported catalysts

As the temperature increases, methane conversion improves for all catalysts, indicating a strong temperature dependence of the steam reforming reaction. Among the catalysts, $Ni/CeO_2$ consistently shows the highest methane conversion, suggesting its superior activity, followed closely by $Co/CeO_2$. $La/CeO_2$ and $Fe/CeO_2$ exhibit slightly lower conversions but still follow a similar trend of increasing conversion with temperature. These results highlight the importance of the active metal in determining the efficiency of steam methane reforming, with nickel demonstrating the best catalytic performance. CO selectivity is high for $Ni/CeO_2$ catalyst as compared to others. [36] Therefore, CO selectivity can be reduced by adding promoters to Ni based catalyst with both alumina and ceria supports as shown in Fig 3.7 and 3.8.

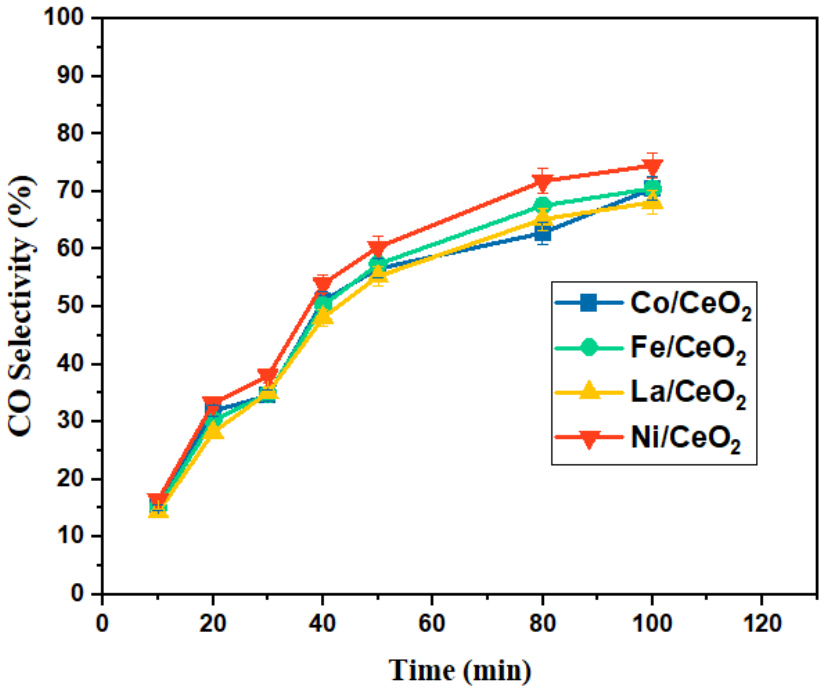


**Fig. 3.8** CO selectivity vs time graph of monometallic ceria supported catalysts

$CO_2$ selectivity of all the catalysts is high as compared to Ni based catalyst on both alumina and ceria supports. Therefore, Fe, La, Co is used as indicator with $Ni/ Al_2O_3$ as well as

$Ni/CeO_2$ to get high $CO_2$ selectivity. These graphs compare the performance and stability of catalysts supported on $Al_2O_3$ (left graph) and $CeO_2$ (right graph) during steam methane reforming. The left graph as shown in Fig 3.9 shows the $CO_2$ selectivity (%) over time for $Ni/Al_2O_3$, $Co/Al_2O_3$, $La/Al_2O_3$, and $Fe/Al_2O_3$. $Ni/Al_2O_3$ initially achieves the highest methane conversion but rapidly deactivates, likely due to coking or sintering of active sites but less $CO_2$ selectivity.

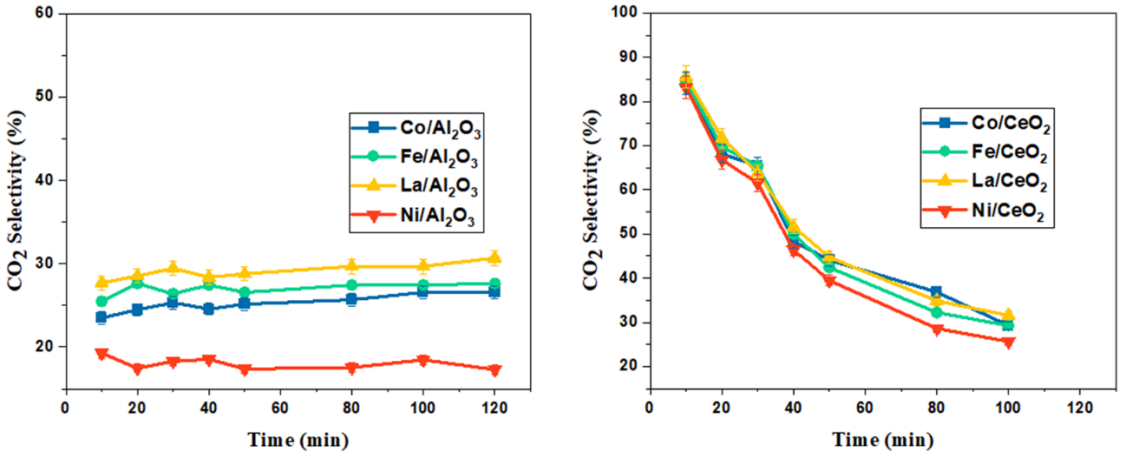


**Fig. 3.9** $CO_2$ selectivity vs time graph of (a) monometallic alumina supported (b) monometallic ceria supported

In contrast, the right graph illustrates the performance of $Ni/CeO_2$, $Co/CeO_2$, $La/CeO_2$, and $Fe/CeO_2$, all of which show a gradual decline in $CO_2$ selectivity over time. $Ni/CeO_2$ achieves the highest conversion and better stability, indicating the beneficial role of $CeO_2$ in enhancing catalytic performance. $Co/CeO_2$, $La/CeO_2$, and $Fe/CeO_2$ exhibit similar stability trends but lower activity compared to $Ni/CeO_2$. Comparing the two supports, $CeO_2$ significantly improves catalyst stability and maintains higher activity, with $Ni/CeO_2$ emerging as the most promising catalyst for steam methane reforming due to its superior performance and resistance to deactivation.

### 3.4 Summary

The analysis of steam methane reforming performance highlights the superior activity of monometallic Ni-based catalysts, supported on $Al_2O_3$ and $CeO_2$, due to their high methane conversion and enhanced stability. However, challenges such as deactivation and CO selectivity remain critical. CO selectivity is also high with monometallic Ni based catalyst. Therefore, Introducing Ni based bimetallic systems with promoters like Fe, La, and Co can address these issues by synergistically improving catalytic performance. Fe can enhance coke resistance and promote water-gas shift activity, reducing CO selectivity. La improves oxygen storage capacity and thermal stability, while Co increases methane activation and facilitates hydrogen production. A bimetallic Ni-based catalyst with these promoters, supported on $Al_2O_3$ and $CeO_2$, is likely to achieve high methane conversion with minimized CO selectivity, offering an optimal balance of activity, stability, and selectivity for efficient steam methane reforming. We have also checked shape morphology of ceria by synthesizing nanorod and nanocube as ceria is also showing good catalytic activity in monometallic catalysts testing. After that, we have also compared the shape effect with commercial ceria for monometallic catalysts to proceed with the best results.

### 3.5 Effect of Shape morphology on Ceria

The oxygen vacancies and surface oxygen species on ceria enhanced the effective activation and dissociation of methane and water, hence promoting the reforming process while minimizing undesirable side reactions. The synthesis of ceria nanostructures (with a controlled morphology) by a hydrothermal method has gained a lot of attention. The different morphologies expose different crystal planes like nano-rods expose (110) and (100) planes, nano-cubes predominantly expose (220) planes, and nano-particles generally of octahedral shapes expose (111) planes, which is responsible for its high oxygen storage and ease oxygen mobility. The oxygen vacancies formation energies for different crystal

planes are also different. [37] This study investigates the influence of nano-structured ceria support with nickel as a metal catalyst on. The decrease of carbon monoxide, which poisons fuel cell electrodes, is a goal of new catalyst development with improved selectivity for SRM. Carbon monoxide at concentrations more than 10 ppm deactivates platinum-based anodes. Cerium oxide, as an alternative route, has been reported to be suitable as a support for SMR metal oxide catalysts because of its high oxygen storage capacity, while oxygen mobility can improve catalytic stability by preventing metal particle sintering and suppressing the formation of carbonaceous species. Thus, employing the hydrothermal approach, $CeO_2$ nanostructures are generated with preferential exposure to specific crystallographic planes, resulting in variable catalytic activity for some catalytic processes. We demonstrate that modifying the form, and surface/face reconstruction of ceria crystallites at the nanoscale, can provide a key tool for controlling activity and selectivity in the SMR process. The effect of ceria forms on steam methane reforming has not been researched yet. In this article, a Ni-based catalyst in various ceria forms, such as nanorods and nanocubes, was synthesized using a hydrothermal technique and investigated for steam methane reforming.

### 3.5.1 Literature review on shape morphology of ceria

Moraes et al. [38] investigated the impact of ceria morphology (nano cubes and nano rods) on the catalytic efficacy of $Ni/CeO_2$ catalysts for the ESR reaction. The ESR activity measurements, done at 300°C over pre-reduced catalysts, revealed that the ceria morphology had no effect on product distribution and that ethanol breakdown and dehydrogenation were the primary processes for all catalyst types. Another study by Araiza et al. investigated the influence of ceria nanostructures (particles, rods, and cubes) on carbon deposition. ethanol steam reforming over 10% $Ni/CeO_2$ catalysts. [39] Nickel supported on ceria nanorods demonstrated the highest activity and hydrogen yield in the

ESR reaction at 550°C for 24 h, as well as the lowest quantity of carbon deposits. These properties of the rod-shaped catalyst were attributed to the increased oxygen storage capacity of ceria rods and the higher dispersion of nickel over this final ceria nanostructure. Most recently, Kourtelesis et al. investigated ethanol steam reforming over $Pt/CeO_2$ with various support morphologies. [40] Furthermore, the catalytic performance of the various ceria nano shapes is assessed for the ESR reaction. Table 3.3 represents the research done on shape morphology of ceria.

**Table 3.3** Catalyst shape morphology effect on steam reforming

| **Authors** | **Ceria morphology** | **Catalytic properties** | **Application** | **Key Findings** |
|---|---|---|---|---|
| Yang et al., 2019 [41] | Nanorods | High oxygen storage capacity (OSC), better reducibility | Methanol steam reforming | Ceria nanorods showed superior $H_2$ production due to increased surface area and active sites. |
| Soykal et al., 2012 [42] | Nanocubes | Stable crystal planes, moderate reducibility | Ethanol steam reforming | Cubic ceria supported better stability, minimizing carbon deposition. |
| Li et al., 2022 [43] | Nanopolyhedra | Balanced OSC, exposure of multiple active facets | Biogas reforming | Polyhedral ceria enhanced syngas yield by promoting uniform gas distribution. |
| Wang et al., 2023 [44] | Hierarchical Ceria | Large accessible surface areas | Glycerol steam reforming | Hierarchical structures reduced sintering and deactivation during long-term use. |

| | | | | |
|---|---|---|---|---|
| Araiza at al., 2020 [39] | Nanorods, other morphologies | Reduced carbon deposition and improved catalyst stability | Ethanol steam reforming | Specific ceria morphologies (e.g., nanorods) reduce carbon formation and enhance catalyst stability in ethanol steam reforming. |
| Gao et al., 2022 [45] | Hierarchical structure | Enhanced methane conversion and reduced carbon deposition | Dry reforming of methane | Hierarchical ceria structures improve Ni-based catalyst performance by enhancing methane conversion and minimizing carbon deposition. |
| Vecchietti et al., 2022 [48] | Nanoparticles (shape-controlled) | Enhanced hydrogen production with controlled shape effects | Ethanol steam reforming | Shape-controlled ceria nanoparticles enhance hydrogen production in ethanol steam reforming by promoting efficient ethanol decomposition and hydrogen formation. |
| Moraes et al., 2015 [38] | Nanoparticles, other shapes | Enhanced catalyst performance, lower activation energy, and high ethanol conversion | Low-temperature steam reforming of ethanol | Ceria morphology influences Ni/$CeO_2$ catalysts, leading to lower activation energy and high ethanol conversion at low temperatures. |

Very few literatures reported on ceria morphology study particularly for steam methane reforming. Ceria morphology can affect the conversion, CO selectivity in steam methane reforming.

### 3.5.2 Catalyst characterization

The surface area determination of all the prepared powder supports and catalysts was performed using Brunauer–Emmett–Teller (BET) analysis and the pore volume was determined by using the Barrett–Joyner–Halenda (BJH) model from $N_2$ adsorption–desorption isotherms at 77 K, degassing at 473 K for 2 h using Meso 112 (Altamira Instruments, Inc.). The crystal size and structure of all the powder supports and catalysts were determined by an X-ray diffraction (XRD) pattern recorded with a Cu kα (100 mA and 40 kV) radiation in the 3 to 80̊ diffraction range, using an X-ray powder diffractometer (Rigaku Mini flex 600 X-Ray Diffraction System, RIGAKU Corporation) with a Cu Kα radiation source at (λ = 1.5418 Å). The XRD analysis ranged with a scan rate of 10/min and a step size of 0.02, and the average crystal size of the samples was calculated using the Scherrer equation. The analysis of nanoparticle shape and size was obtained by transmission electron microscopy (TEM) operated at an accelerating voltage of 200 kV using a field emission source equipped JEOL JEM-2100 electronic microscope. The morphologies of the reduced and spent catalysts were characterized using transmission electron microscopy. The sample for TEM analysis was prepared by dispersing 0.1 g of catalyst powder in 10 mL ethanol and then sonicating for 1 h in an ultrasonic bath until the catalyst was completely dispersed. Then one drop of this dispersed solution was drop-casted on a carbon-coated copper grid and put in a hot air oven for drying. The surface morphology and elemental analysis were done by energy dispersive X-ray spectroscopy (EDS) analysis where the samples were sputtered with a thin gold film to decrease the

charging property using a SEM: EVO 18-20-45 instrument and the (EDS) analysis was done.

### 3.5.3 Catalyst synthesis procedure

The hydrothermal method was used to prepare all the ceria supports. $CeO_2$ nanorods and nano cubes were produced. Cerium (III) nitrate hexahydrate (99.5% purity, Thermo Scientific) as a ceria salt, sodium hydroxide pellets (>97%, Qualigens), urea (99%, Qualigens), and nickel (II) nitrate hexahydrate (>98%, EMPLURA) as a metal salt were taken as precursors. For ceria nanorods and ceria nanocubes, 2.298 mmol, 7.998 mmol $Ce(NO_3)_3.6H_2O$, and 300 mmol, 800 mmol NaOH were dissolved in 50 mL, 80 mL of deionized water, respectively. The solution was continuously stirred at room temperature (303 K) until it turned into purple and white slurry, and then this slurry was transferred into a 100 mL Teflon-lined stainless-steel autoclave and kept in a hot-air oven for 24 h at 393 and 428 K, respectively. After the hydrothermal synthesis, the mixture was cooled down to room temperature, and the precipitate was separated from the aqueous solution by centrifugation. After the hydrothermal treatment, the precipitates were filtered using ethanol and deionized water several times. The filtrate was kept for drying in a hot-air oven for 12 h at 353 K. Finally, the synthesized ceria nanorods and nanocubes were calcined for 6 h at 823 K. [46] To prepare the supported nickel catalyst, ceria nanorods and ceria nanocubes were doped with nickel (5 wt.% metal loading) by the wet impregnation method using nickel nitrate hexahydrate as a metal precursor salt.

### 3.5.4 Catalyst performance in packed bed reactor

The equipment used for testing catalysts for steam methane reforming is a fixed bed reactor made of Inconel. This catalytic testing unit includes a packed bed reactor with an internal diameter of 11.74 mm and a length of 682 mm, an electric furnace with two heating zones,

two K-type thermocouples, a feed pump, vaporizer, pre-mix heater, condenser, gas–liquid separator, and mass flow controllers. Asbestos is utilized as the catalyst bed base in a packed bed reactor with 0.77 g of produced catalyst loaded along with identical-sized inert (quartz) in a 1:1 ratio. Prior to the catalyst loading, the catalyst is sieved in the range of 180–300 μm. To measure the temperature inside the reactor, the K-type thermocouple is inserted from the top. In the presence of a nitrogen flow rate of 50 mL/min, the reactor temperature is increased to 850°C, and the catalyst is then reduced in situ for 2 h in the presence of hydrogen at 850°C. The temperature is then lowered to reaction temperatures ranging from 550 to 800°C. The preheated steam and methane are fed to the reactor maintained at the reaction temperature. The product gases are then passed through a condenser where unreacted steam gets condensed and then passed through a gas–liquid separator where condensed liquid and gaseous product get separated. The experimental data are recorded every 30 min during the catalytic performance evaluation tests. The composition of separated gaseous product is analyzed with gas chromatography (CENTURION SCIENTIFIC) containing two columns: a molecular sieve and a Porapak Q along with TCD (thermal conductivity detector). The catalyst activity for the SMR reaction was evaluated in terms of methane conversion, CO selectivity, and $CO_2$ selectivity.

## 3.6 Results and discussion

### 3.6.1 BET and XRD

Table 3.4 shows the BET surface area, pore volume, and average pore diameter data of ceria support of different morphologies and nickel-doped ceria support obtained by BET analysis. The surface area of the catalysts is calculated by the BET equation, pore volume, and the pore diameters are calculated by the BJH method. To evaluate the physical properties of the catalyst samples, $N_2$ adsorption desorption experiments are carried out, and the results are shown in Figure 3.10. It depicts the $N_2$ adsorption–desorption isotherms

of the synthesized catalysts, which shows significant changes in pore structure when the $CeO_2$ supports has varied morphologies. The surface area of the ceria nanorod and nanocube calcined at 550℃ is 75.179 and 14.922 $m^2/g$ respectively, whereas the surface area of the ceria nanorod and nanocube calcined at 970℃ dropped to 10.461 and 3.473 $m^2/g$, respectively. This shows that high temperature calcination blocks the pores of both the nanorod and nanocube. The pore blocking is more significant in the nanorod compared to the nanocube. However, the pore blocking alone cannot lead to such a dramatic change in surface area and this may be associated to the change in shape itself.

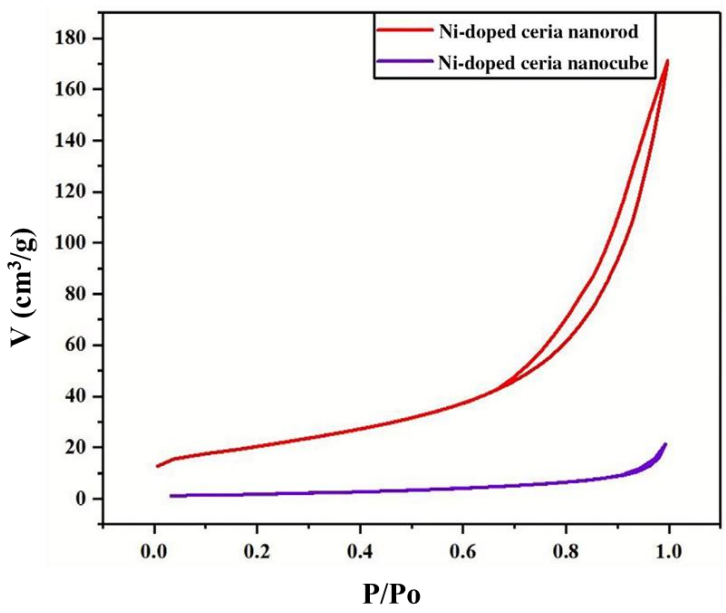


**Fig. 3.10** Brunauer–Emmett–Teller (BET) $N_2$ adsorption desorption isotherm of Ni-doped ceria nanorod and nanocube calcined at 550°C

After nickel doping, the surface area and pore volume of the ceria nanorod and nanocube get reduced to 73.416 and 4.174 $m^2/g$, respectively, due to the blocking of pores. The Ni metal particles get deposited into the pores, which increased the pore diameter of the catalyst in the nanocube. The pore volume also gets reduced, which confirms the deposition of metal particles into the pores.

When the calcination temperature increases, the pore volumes of both the nanorod and the nanocube reduce. The reduction is more pronounced in the case of the nanorod compared to the nanocube. This may be associated with the shape transformation of the nanorod that can be seen in the TEM images, which resulted in the pore collapse. All of the produced catalysts exhibited IV-type isotherms, which were primarily obtained from mesoporous adsorbent materials. H2-type hysteresis loops are typically created by porous sorbents or homogenous particle accumulation pores, indicating the synthesis of a regular mesoporous structure within the manufactured catalysts. Furthermore, the occurrence of an H3-type hysteresis loop at higher relative pressures (p/p0> 0.6), which is typically produced by mesoporous or macroporous materials with broad and diffuse slit like pores, demonstrates the irregular pore structure and wide pore size distribution. [47] Among all the catalysts, the ceria nanorod calcined at 550℃ has the best hysteresis loop, indicating that ceria support can aid in the production of mesopores and large pores. It is worth mentioning that nanorod calcined at 550℃ exhibited the highest specific surface area and pore volume, most well-developed pore structure.

**Table 3.4** BET surface area, pore volume and pore diameter of different catalysts

| Samples | BET surface area ($m^2/g$) | Pore volume ($cm^3/g$) | Average pore size (nm) |
|---|---|---|---|
| Ceria nanorod support calcined at 550°C | 75.179 | 0.284 | 9.783 |
| Ceria nanocube support calcined at 550°C | 14.922 | 0.324 | 10.134 |
| Ceria nanorod support calcined at 970°C | 3.473 | 0.010 | 11.070 |
| Ceria nanocube support calcined at 970°C | 10.461 | 0.170 | 12.136 |
| Nickel-doped nanorod calcined at 550°C | 3.416 | 0.231 | 5.357 |
| Nickel-doped nanocube calcined at 550°C | 4.174 | 0.287 | 16.788 |

Figure 3.11 represents the XRD pattern of the ceria nanorod and nanocube calcined at 550 and 970°C with and without metal doping. As can be observed from the XRD graph, all the catalysts show the cubic fluorite structure of ceria (JCPDS 89-2529). The diffraction peaks of 5% Ni/$CeO_2$ at 28.35, 33.43, 36.31, 57.42, 58.12, 69.45, and 76.56° correspond to (111) (200) (111) (311) (222) (400) (331) crystal planes, respectively. The $CeO_2$ nanorods and nanocubes belong to the pure cubic phase with space group Fm-3m. The ceria nanorod samples calcined at 970°C show sharp crystalline peaks as compared to the ceria nanorod samples calcined at 550°C. These sharp peaks of samples calcined at 970°C show a high degree of crystallinity. This also shows a large crystal size. Moreover, the peaks at 33.43° and 36.31° show impregnation of NiO. Table 3.5 shows the crystal size calculated by using the Scherer equation using XRD data. The crystal size of Ni-doped ceria nanorod calcined at 550 and 970°C was calculated as 9.82 nm and 91.05 nm, respectively. The crystal size of the Ni doped $CeO_2$ nanocubes calcined at 550 and 970°C is 55.29 and 77.59 nm, respectively. This shows that NiO dispersion in doped ceria nanorods calcined at 550°C is better than other cases. Further, the increase in calcination temperature from 550 to 970°C increases the peak

intensity for both the nanorod and nano-cube (as shown in Fig 3.11 b, d). This implies an increase in crystallinity caused by an increase in the crystalline volume ratio as the nuclei grew in size. The FWHM of the diffraction peaks decreases as crystallite grows. As it can be seen from Table 3.5 that the crystal size of both the shapes increases when calcined at 970°C. However, the XRD data also confirms a sharp change in peak intensity and crystal size in the case of the nanorod when the calcination temperature increases from 550 to 970°C. This is due to change in the shape of the nanorod at a high temperature.

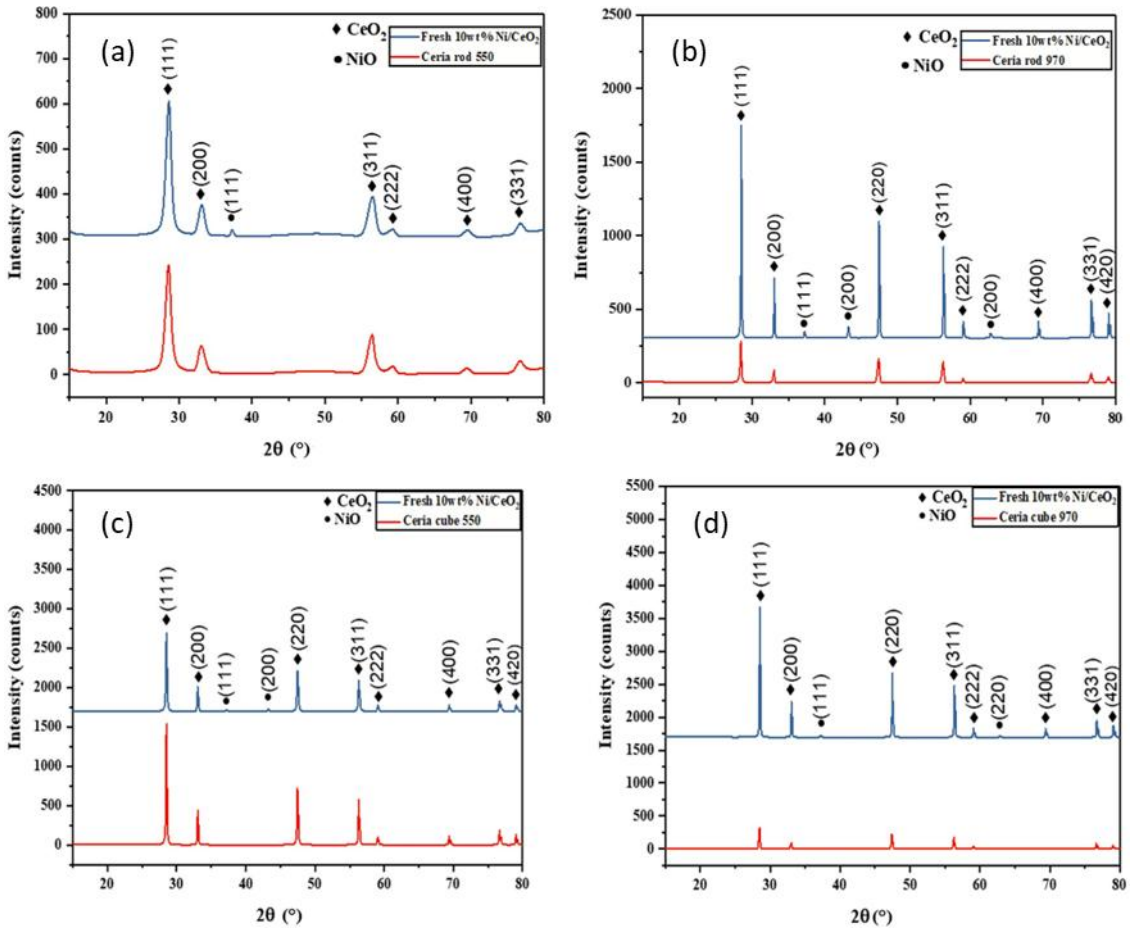


**Fig. 3.11** X-ray diffraction (XRD) analysis of Ni doped ceria (a) nanorod calcined at 550°C, (b) nanorod calcined at 970°C, (c) nanocube calcined at 550°C, and (d) nanocube calcined at 970°C

### 3.6.2 TEM/EDX Results

Fig 3.12 (a-d) shows the TEM images of nickel-doped ceria nanorod and nanocube fresh catalysts calcined at 550 and 970˚C. The nanoparticles presented in Fig 3.12a shows a rod shape oriented in different directions. Selected area diffraction (SAED) images show polycrystalline structure for all the four cases. The particle sizes of nanorod calcined at 550˚C range from 60 to 220 nm, with an average particle size of 130 nm. The TEM image of the ceria nanocube calcined at 550˚C (Fig 3.12b) shows a cube-shaped microstructure orientated along the [220] zone axis of the fluorite-type structure, with small truncations revealing (110) facets. [48] The size of nanocube calcined at 550˚C varies from 120 to 220 nm with a mean of 175 nm. This shows that the mean particle size of nanocube is bigger than the nanorod. However, the particle size distribution in the case of the nanorod is wide. Fig 3.12 (c-d) shows that with an increase in calcination temperature from 550 to 970˚C, the morphologies of both the nanorod and the nanocube change.

In the case of nanocube (Fig 3.12d), the shape remains almost the same; however, the particle size reduces due to sintering at high temperature. The particle size in the case of the nanocube calcined at 970˚C ranges from 100 to 200 nm with a mean size of 140 nm. The same was also observed from the BET surface area measurement, which shows a reduction in the surface area and pore volume with an increase in the calcination temperature due to pore blockage, which might have initiated due to sintering. However, in the case of the nanorod (Fig 3.12c) the shape of the nanorod at 970˚C changes from nanorod to more or less like the nanocube.

**Table 3.5** Crystallite sizes of various ceria shape morphologies

| Ceria support | Crystallite size (nm) before Ni doping | Crystallite size (nm) after Ni doping |
|---|---|---|
| **Nano-cube calcined at 550°C** | 32.47 | 55.29 |
| **Nano-cube calcined at 970°C** | 55.84 | 77.59 |
| **Nano-rod calcined at 550°C** | 8.32 | 9.82 |
| **Nano-rod calcined at 970°C** | 42.28 | 91.05 |

The particle size of the nanorod also reduces at 970°C from a mean size of 130 nm at 550°C to a mean size of 95 nm. Similar observations are made through BET and XRD measurements, which show low surface area, pore volume, and high peak intensity. These results confirm that the nanorod is not stable at a high temperature and its morphology changes close to the nanocube when used at a high temperature. The SAED images of all the catalysts confirm the polycrystallinity. In the case of ceria nanorods calcined at 550°C, at least five distinct diffraction rings are observed.

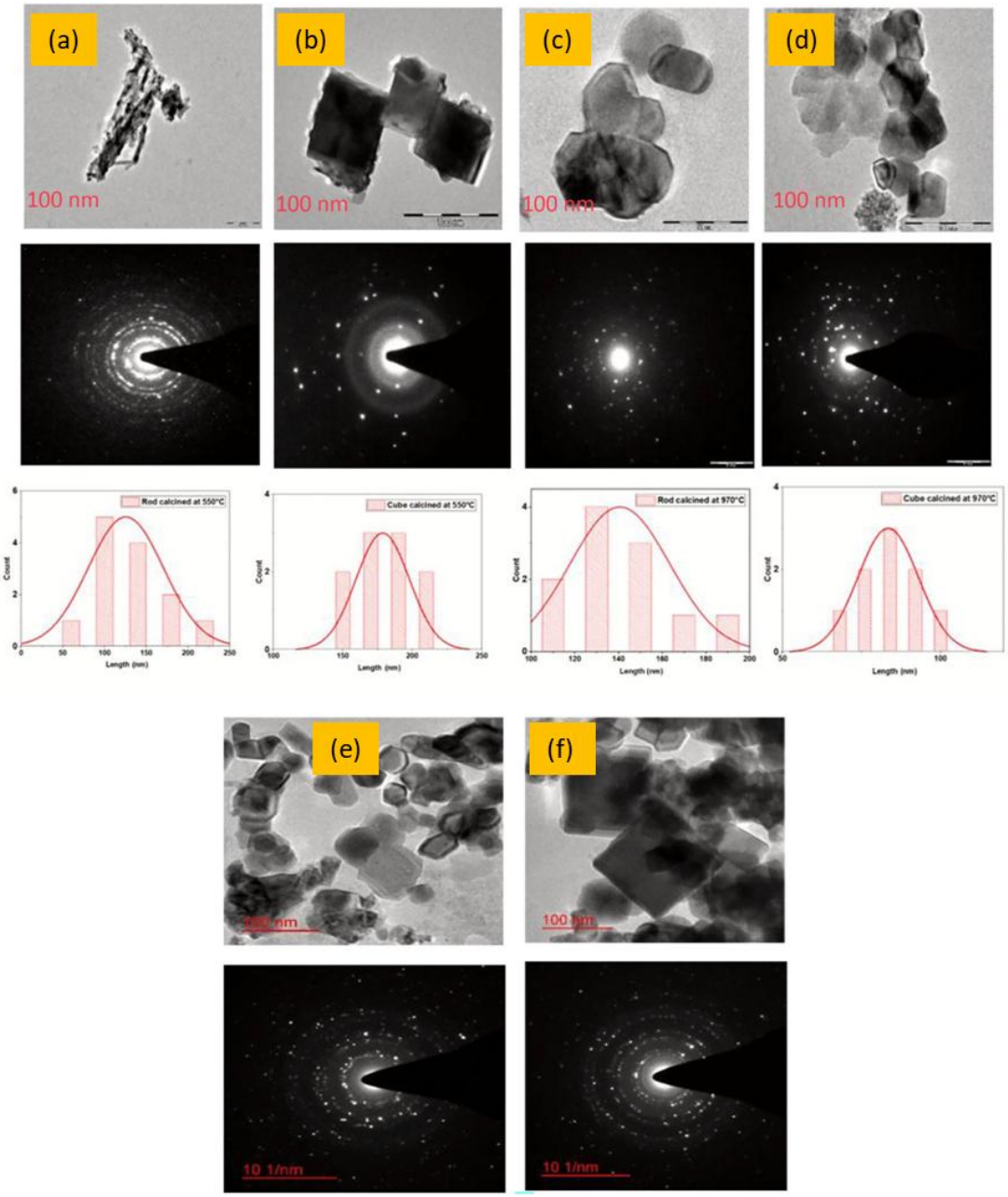


**Fig. 3.12:** Transmission electron microscopy (TEM) image of Ni-doped ceria support. (a) Nanorod calcined at 550˚C, (b) nanocube calcined at 550˚C, (c) nanorod calcined at 970˚C, (d) nanocube calcined at 970˚C, (e) spent nanorod catalyst calcined at 550˚C and reduced at 850˚C, and (f) spent nanocube calcined at 550˚C reduced at 850˚C.

It is significant to notice that the SAED patterns for all the catalysts do not show any clear rings that indicate metallic cerium or other cerium oxides only. The same is

observed through energy dispersive x-ray (EDX) results shown in Fig 3.13. Therefore, these results are also in agreement with EDX results. The spent catalysts of both the ceria nanorod and nanocube calcined at 550°C and reduced at 850°C in the presence of hydrogen is also analyzed by TEM. Fig 3.13 (e-f) shows the TEM images for the spent nanorod and nanocube, respectively. It is observed that the ceria nanorod shape is distorted to more or less like the nanocube, as observed when calcined at 970°C. However, the shape of the nanocube remains same. These results confirm that not only calcination but also reduction at a high temperature affects the nanorod surface morphology. Fig 3.13 (a-b) shows EDX analysis of the Ni-doped ceria nanocube and nanorod-shaped catalysts calcined at 550°C. It shows that for both the cases Ce, O, and Ni are present in the samples. Nickel is well dispersed on the surface of the catalysts for both the cases. However, this reaction might result in the production of carbon deposits on the catalyst surface, deactivating the catalyst over time. This results in reduced efficiency and higher expenses due to catalyst replacement or regeneration. Pashchenko and Makarov [49] also reported carbon deposition by calculating carbon deposition by formula given below

$$M_{\text{Carbon}} = M_{\text{spent catalyst}} - M_{\text{before catalyst}}$$

In our study, we have also calculated the mass of deposited carbon by this formula. No gain in weight was observed in spent catalyst. It is confirmed that carbon formation was not there in the catalyst during reaction. [49] It was also confirmed by TEM images of spent catalysts as represented in Fig 3.13 (e-f). In this study, ceria is used as a support. Because of its redox activity, ceria can engage in oxygen transfer reactions, giving and receiving oxygen atoms as needed to enhance the oxidation of carbonaceous species and prevent the buildup of carbon. [50]

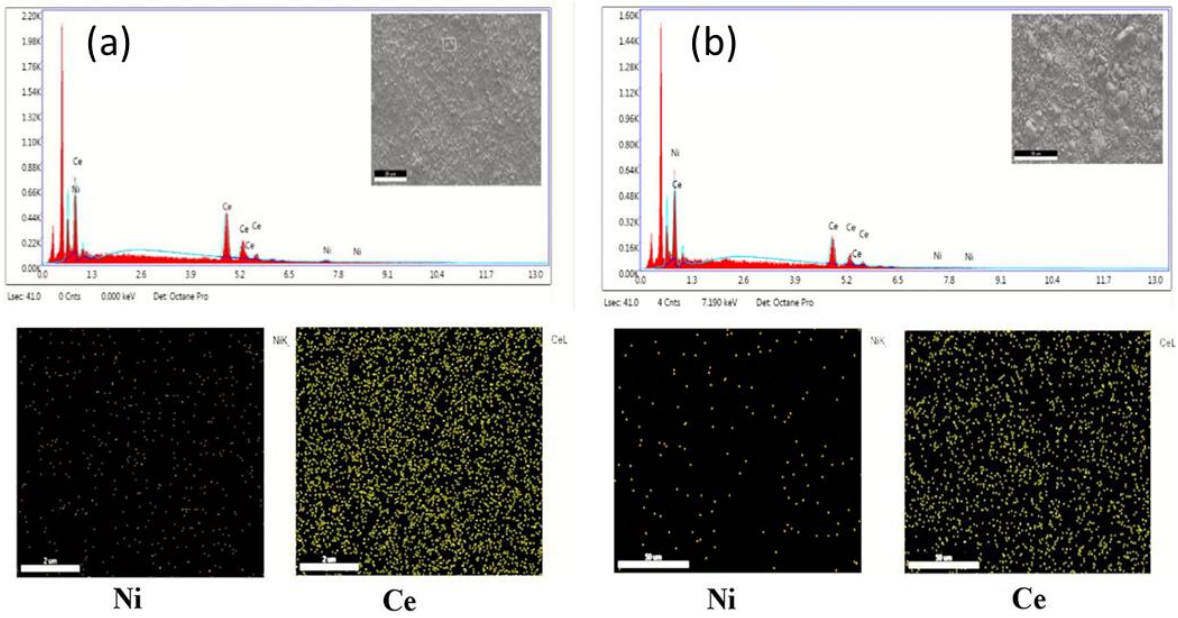


**Fig. 3.13** EDX analysis of (a) Ni-doped nano cube calcined at 550˚C and (b) Ni-doped nano rod calcined at 550˚C as received (blue line) and as implanted (red line).

### 3.6.3 Experimental results

**Methane conversion**

Fig 3.14 shows methane conversion versus time graph for the ceria nanorod and nanocube calcined at 550˚C. It can be seen from the graph that conversion for both the ceria nanorod and nanocube increases with the increase in temperature as the reaction is endothermic in nature. At a lower temperature (550˚C), the nanorod gives better conversion than the nanocube. This is mainly due to the higher surface area and lower crystallite and particle size of nanorod compared to the nanocube, which provides better activity. However, with an increase in temperature, the nanocube performs better compared to the nanorod as the shape of the nanorod distorted at a higher temperature, which leads to the lower activity of the catalyst. At higher temperatures (750 and 800˚C), the performance of the nanorod is close to the performance of the nanocube. These results are in line with the TEM analysis, which shows that at a higher temperature, the nanorod shape is distorted to more or less like the nanocube. However,

the nanocube performs better and provides a higher conversion than the nanorod at all the temperatures other than 550˚C.

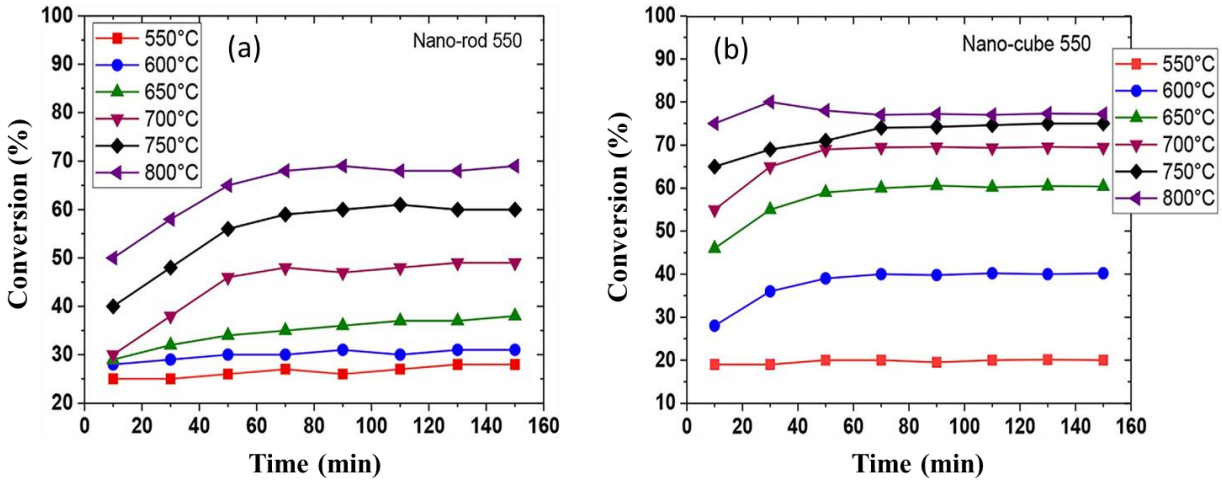


**Fig. 3.14** Conversion versus time graph of (a) nanorod calcined at 550˚C and (b) nanocube calcined at 550˚C

**CO and $CO_2$ selectivity**

Fig 3.15 (a-b) represents the CO selectivity and Fig 3.15 (c-d) represents the $CO_2$ selectivity of the nanorod and nanocube calcined at 550˚C. The CO selectivity of a nanocube calcined at 550˚C can be observed as lower compared to the CO selectivity of a nanorod calcined at the same temperature. The water gas reaction is favorable at low temperatures. An increase in temperature favors the reverse water gas shift reaction to achieve equilibrium, which is also responsible for the increase in CO concentration. [51] Further, at a higher temperature the methane decomposition is also reported. Hence, at a high temperature, both the nanorod and nanocube show higher CO selectivity and lower $CO_2$ selectivity compared to the low temperature.

However, at all the temperatures, the nanocube calcined at 550˚C showed the lower CO selectivity compared to the nanorod. At 800˚C, the nanocube CO selectivity is 40% compared to the 90% CO selectivity in the case of the nanorod calcined at 550˚C. This

means that the nanocube ceria promotes the water gas shift reaction at even higher temperatures. Hence, $CO_2$ selectivity for the nanocube is higher compared to the nanorod at all temperatures. The exposed crystal plane (220) of the ceria nanocube is attributed to the higher $CO_2$ selectivity. [52]

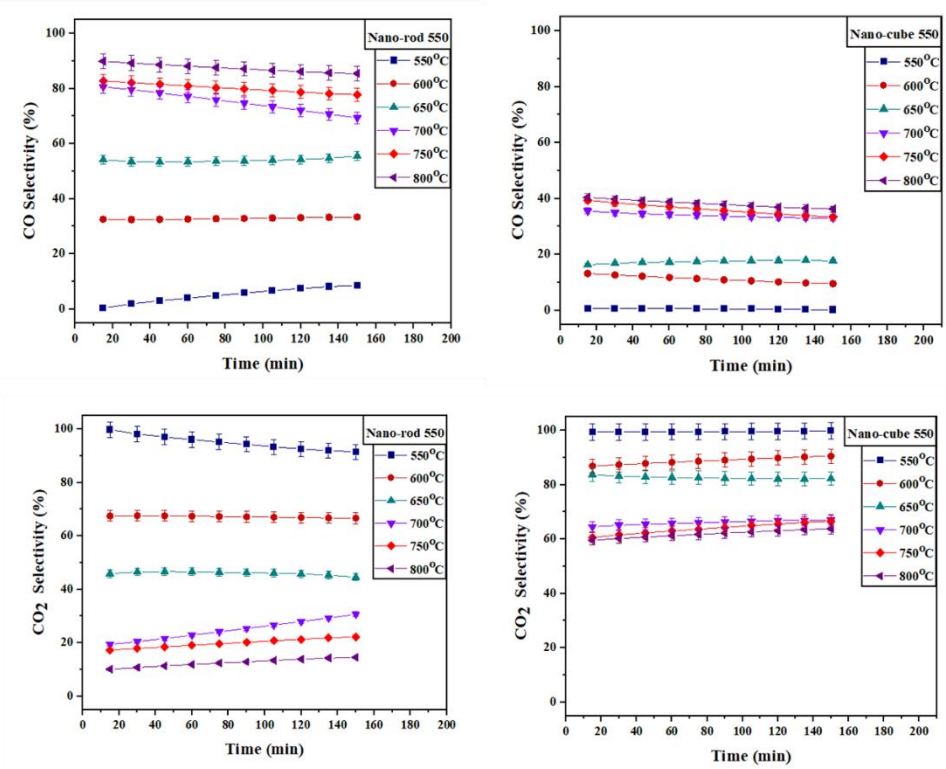


**Fig. 3.15** CO selectivity vs time graph for (a) nanorod calcined at 550°C (b) nanocube calcined at 550°C, $CO_2$ selectivity (c) nanorod calcined at 550°C (d) nanocube calcined at 550°C

### 3.6.4 Comparison with commercial ceria

In this section, nanorod and nanocube catalytic activity is compared with commercial ceria to proceed with further experiments. The effect of calcination temperature is also studied on the activity of the catalyst in terms of conversion and CO selectivity. For comparison, the experiments are performed at 700˚C, which balance the conversion and CO selectivity for all the catalysts, that is, the nanocube, nanorod and commercial ceria. As mentioned earlier, the whole motivation of this work is to find a catalyst that provides higher conversion and low CO selectivity.

**Methane Conversion**

Fig 3.16 (a-b) shows conversion graph of nanorod, nanocube and commercial ceria calcined at 550℃ and 970℃. Fig 3.16 (c-d) shows the CO selectivity of the nanorod and nanocube, when calcined at 550 and 970˚C respectively. In the case of both of the catalysts (nanorod and nanocube), CO selectivity reduces when the calcination temperature increases. The nanocube ceria showed low CO selectivity (34% for calcined at 550˚C, 20% for calcined at 970˚C) as compared to the nanorod CO selectivity (75% calcined at 550˚C, 18% calcined at 970˚C). The reduction in CO selectivity is prominent in the case of the nanorod compared to the nanocube. This can be explained through the change in the shape of the nanorod when calcined at a higher temperature and significant increase in peak intensity for the (111) plane. In SMR, methane get adsorbed on the Ni site while water is dissociatively adsorbed on the ceria (111), (100), and (200) planes. [53-54] but CO selectivity of commercial ceria is lower for both the calcination temperature with maximum conversion as compared to both the shapes. Our goal is to get maximum conversion at low temperature with low CO selectivity. As commercial ceria is better than both the shapes in fulfilling the objective, commercial ceria will be used for further experiments.

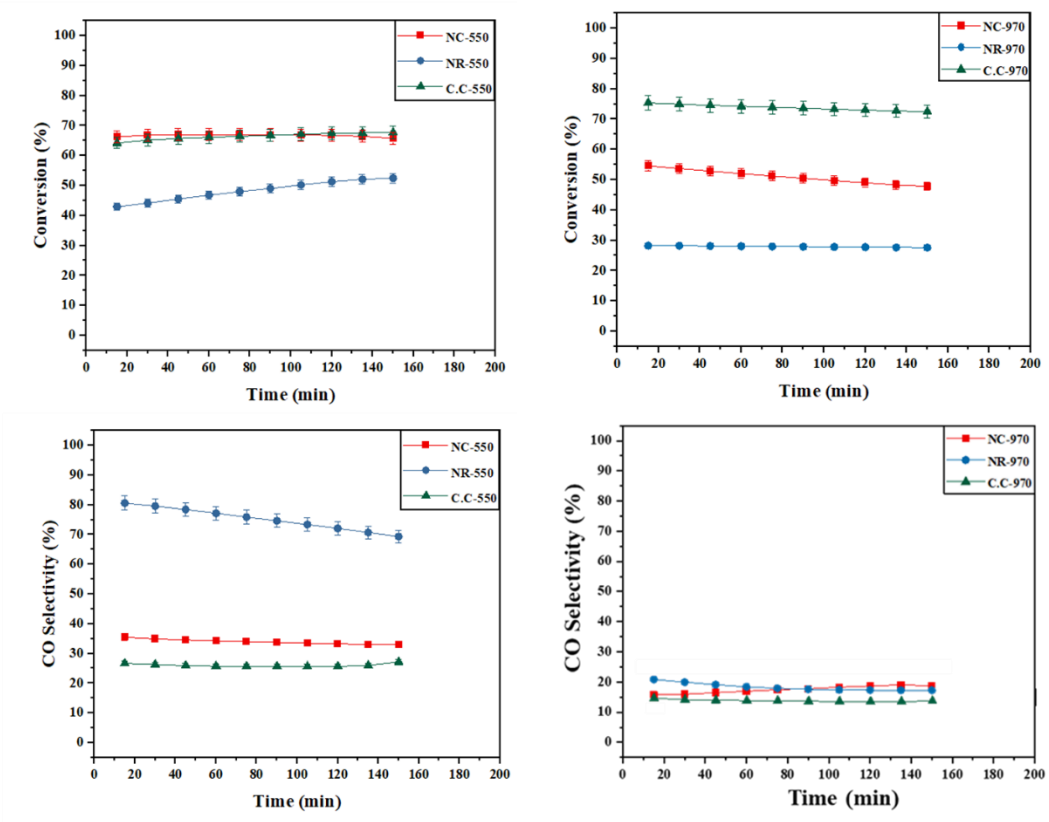


**Fig. 3.16** Comparison of commercial ceria with different shapes (a) conversion graph of samples calcined at 550℃ (b) conversion graph of samples calcined at 970℃ (c) CO selectivity graph of samples calcined at 550℃ (d) CO selectivity graph of samples calcined at 970℃

### 3.7 Conclusions

In this study, activity of monometallic catalysts supported on alumina and ceria is tested in a packed bed reactor for steam methane reforming, targeting high conversion and low CO selectivity. Nickel based monometallic catalysts supported on both alumina and ceria showed high catalytic activity. Therefore, before proceeding with further experiments, shape effect of ceria is also checked with nanorod and nanocube. It was found that the nanocube gives better conversion at a high temperature while the nanorod gives higher conversion at a low temperature. The CO selectivity changes significantly with surface morphology. It was found that the CO selectivity of the nanocube is much lower than the nanorod. In summary, it can be concluded that the

reduction temperature, calcination temperature, and different morphologies of ceria affect the catalytic activity for steam methane reforming in terms of conversion, CO selectivity, $CO_2$ selectivity. When these shapes results compared with commercial ceria results, high conversion with low CO selectivity is observed with commercial ceria. As high CO selectivity is observed with Nickel based monometallic catalyst on both alumina and ceria. Further experiments are tested with bimetallic catalyst to get maximum conversion at low temperature with low CO selectivity and high stability without deactivation of catalysts. In chapter 4, In current work, Ni-based alumina and ceria supported catalysts are used. The effect of La and Fe promoters on the performance of Ni-based alumina and ceria supported catalysts are investigated. The catalysts are synthesized using wet impregnation method. A complete characterization of catalysts is performed using BET, XRD, FESEM, and EDX. Fe promoted catalysts shows low CO and high $CO_2$ selectivity which is desirable for membrane reformer. However, the catalytic activity of Fe promoted Ni-based alumina and ceria supported catalysts were low. La promoted Ni-based catalysts show high catalytic activity on both alumina and ceria supported catalysts. La promoted catalysts also gives low start up time, high catalytic activity and low CO selectivity at low temperature. Ni-La/$Al_2O_3$ catalyst provides 50 % conversion and 12% CO selectivity at 500 °C. This makes it suitable for 'on-site' generation of ultra-pure hydrogen through membrane reformer. Moreover, Ni-Co bimetallic also shows high catalytic activity towards steam methane reforming by reducing coke deposition.

**References**


1. Ross, J. R., Steel, M. C., Zeini-Isfahani, A. (1978). Evidence for the participation of surface nickel aluminate sites in the steam reforming of methane over nickel/alumina catalysts. *Journal of Catalysis*, 52(2), 280-290.
2. Zhou, L., Guo, Y., Zhang, Q., Yagi, M., Hatakeyama, J., Li, H., Kameyama, H. (2008). A novel catalyst with plate-type anodic alumina supports, $Ni/NiAl_2O_4/\gamma\text{-}Al_2O_3$/alloy, for steam reforming of methane. *Applied Catalysis A: General*, 347(2), 200-207.
3. Boukha, Z., Jiménez-González, C., de Rivas, B., González-Velasco, J. R., Gutiérrez-Ortiz, J. I., López-Fonseca, R. (2014). Synthesis, characterisation and performance evaluation of spinel-derived $Ni/Al_2O_3$ catalysts for various methane reforming reactions. *Applied Catalysis B: Environmental*, 158, 190-201.
4. Seman, M. H. A., Othman, N. H., Osman, N., Jani, A. M. M. (2023). Nickel based catalysts supported on porous support for methane steam reforming: potential and short review. In IOP Conference Series: *Earth and Environmental Science*, 1151(1), 012061.
5. Seo, J. G., Youn, M. H., Song, I. K. (2010). Mesoporous nickel–alumina catalysts for hydrogen production by steam reforming of liquefied natural gas (LNG). *Catalysis surveys from Asia*, 14, 1-10.
6. Ali, S., Al-Marri, M. J., Abdelmoneim, A. G., Kumar, A., Khader, M. M. (2016). Catalytic evaluation of nickel nanoparticles in methane steam reforming. *International Journal of Hydrogen Energy*, 41(48), 22876-22885.
7. Busca, G., Spennati, E., Riani, P., Garbarino, G. (2024). Properties, Industrial Applications and Future Perspectives of Catalytic Materials Based on Nickel and Alumina: A Critical Review. *Catalysts*, 14(8), 552.
8. Salcedo, A., Lustemberg, P. G., Rui, N., Palomino, R. M., Liu, Z., Nemsak, S.,

Irigoyen, B. (2021). Reaction pathway for coke-free methane steam reforming on a Ni/$CeO_2$ catalyst: active sites and the role of metal–support interactions. *ACS catalysis*, 11(13), 8327-8337.

9. Wu, C., Xiao, Z., Wang, L., Li, G., Zhang, X., Wang, L. (2021). Modulating oxidation state of Ni/$CeO_2$ catalyst for steam methane reforming: a theoretical prediction with experimental verification. *Catalysis Science & Technology*, 11(5), 1965-1973.
10. Lustemberg, P. G., Mao, Z., Salcedo, A., Irigoyen, B., Ganduglia-Pirovano, M. V., Campbell, C. T. (2021). Nature of the active sites on Ni/$CeO_2$ catalysts for methane conversions. *ACS catalysis*, 11(16), 10604-10613.
11. Liu, Z., Yao, S., Johnston-Peck, A., Xu, W., Rodriguez, J. A., Senanayake, S. D. (2018). Methanol steam reforming over Ni-$CeO_2$ model and powder catalysts: Pathways to high stability and selectivity for $H_2$/$CO_2$ production. *Catalysis Today*, 311, 74-80.
12. Xu, W., Liu, Z., Johnston-Peck, A. C., Senanayake, S. D., Zhou, G., Stacchiola, D., Rodriguez, J. A. (2013). Steam reforming of ethanol on Ni/$CeO_2$: reaction pathway and interaction between Ni and the $CeO_2$ support. *ACS Catalysis*, 3(5), 975-984.
13. Thattai, A. T., van Biert, L., Aravind, P. V. (2017). On direct internal methane steam reforming kinetics in operating solid oxide fuel cells with nickel-ceria anodes. *Journal of Power Sources*, 370, 71-86.
14. Ricca, A., Palma, V., Martino, M., Meloni, E. (2017). Innovative catalyst design for methane steam reforming intensification. *Fuel,* 198, 175-182.
15. Sá, S., Silva, H., Brandão, L., Sousa, J. M., M endes, A. (2010). Catalysts for methanol steam reforming-A review. *Applied Catalysis B: Environmental*, 99(1-2), 43-57.
16. Iglesias, I. D., Baronetti, G. T., Mariño, F. J. (2017). Behavior of Coprecipitated $NiAl_2O_4$/$Al_2O_3$ Catalysts for Low-Temperature Methane Steam Reforming. *Energy*

*Sources, Part A: Recovery, Utilization, and Environmental Effects*, 39(2), 129-133.

17. Hou, K., Hughes, R. (2001). Steam reforming of methane over nickel-aluminum spinel-derived catalyst. *Chemical Engineering Journal*, 82(3), 311-328.
18. Baudh, A., Garjola, M., Sharma, R., Sharma, S., Upadhyay, R. K. (2024). Effect of ceria morphology on hydrogen production via methane steam reforming for membrane reformer. *The Canadian Journal of Chemical Engineering*.
19. Patel, A., Kumar, S., Mehta, R. (2020). $Ni/Al_2O_3$ catalyst for methane steam reforming: Performance and cost-effectiveness. *Journal of Catalysis Research*, 15(3), 212–220.
20. Pant, K. K., Jain, R., Jain, S. (2011). Renewable hydrogen production by steam reforming of glycerol over $Ni/CeO_2$ catalyst prepared by precipitation deposition method. *Korean Journal of Chemical Engineering*, 28, 1859-1866.
21. Saraswat, S. K., & Pant, K. K. (2013). Synthesis of hydrogen and carbon nanotubes over copper promoted Ni/SiO2 catalyst by thermocatalytic decomposition of methane. *Journal of Natural Gas Science and Engineering*, 13, 52-59.
22. Ross, J. R. H., & Steel, M. C. F. (1973). Mechanism of the steam reforming of methane over a coprecipitated nickel-alumina catalyst. *Journal of the Chemical Society*, Faraday Transactions 1: Physical Chemistry in Condensed Phases, 69, 10-21
23. Salcedo, A., Lustemberg, P. G., Rui, N., Palomino, R. M., Liu, Z., Nemsak, S., Irigoyen, B. (2021). Reaction pathway for coke-free methane steam reforming on a $Ni/CeO_2$ catalyst: active sites and the role of metal–support interactions. *ACS catalysis*, *11*(13), 8327-8337.
24. Kumar, R., Kumar, K., Pant, K. K., & Choudary, N. V. (2020). Tuning the metal-support interaction of methane tri-reforming catalysts for industrial flue gas utilization. *International journal of hydrogen energy*, 45(3), 1911-1929.

25. Greluk, M., Gac, W., Rotko, M., Słowik, G., Turczyniak-Surdacka, S. (2021). Co/$CeO_2$ and Ni/$CeO_2$ catalysts for ethanol steam reforming: Effect of the cobalt/nickel dispersion on catalysts properties. *Journal of Catalysis*, 393, 159-178.
26. Bozdağ, A. A., Sezgi, N. A., Doğu, T. (2022). Effects of synthesis route on the performance of mesoporous ceria-alumina and ceria-zirconia-alumina supported nickel catalysts in steam and autothermal reforming of diesel. *International Journal of Hydrogen Energy*, 47(7), 4568-4583.
27. Daroughegi, R., Meshkani, F., Rezaei, M. (2020). Characterization and evaluation of mesoporous high surface area promoted Ni-$Al_2O_3$ catalysts in $CO_2$ methanation. *Journal of the Energy Institute*, 93(2), 482-495.
28. Luisetto, I., Tuti, S., Battocchio, C., Mastro, S. L., Sodo, A. (2015). Ni/$CeO_2$–$Al_2O_3$ catalysts for the dry reforming of methane: the effect of $CeAlO_3$ content and nickel crystallite size on catalytic activity and coke resistance. *Applied Catalysis A: General*, 500, 12-22.
29. Trovarelli, A. (1996). Catalytic properties of ceria and $CeO_2$-containing materials. *Catalysis Reviews*, 38(4), 439-520.
30. Miceli, P., Bensaid, S., Russo, N., Fino, D. (2015). Effect of the morphological and surface properties of $CeO_2$ based catalysts on the soot oxidation activity. *Chemical Engineering Journal*, 278, 190-198.
31. Fornasiero, P., Balducci, G. A. B. R. I. E. L. E., Di Monte, R. O. B. E. R. T. A., Kašpar, J., Sergo, V. A. L. T. E. R., Gubitosa, G.,Graziani, M. (1996). Modification of the redox behaviour of $CeO_2$ Induced by structural doping with $ZrO_2$. *Journal of Catalysis*, 164(1), 173-183.
32. Ay, H. (2014). Carbon dioxide reforming of methane on Ni-based bimetallic catalyts.
33. Cassinelli, W. H., Feio, L. S. F., Araujo, J. C. S., Hori, C. E., Noronha, F. B., Marques,

C. M. P., Bueno, J. M. C. (2008). Effect of $CeO_2$ and $La_2O_3$ on the Activity of $CeO_2$− $La_2O_3$/$Al_2O_3$ Supported Pd Catalysts for Steam Reforming of Methane. *Catalysis letters*, 120, 86-94.

34. Profeti, L. P., Ticianelli, E. A., Assaf, E. M. (2008). Co/$Al_2O_3$ catalysts promoted with noble metals for production of hydrogen by methane steam reforming. *Fuel*, 87(10-11), 2076-2081.
35. Baudh, A., Sharma, R., Sharma, S., Kumar Upadhyay, R. (2024). Effect of Lanthanum and Iron Doping on Nickel-Based Alumina and Ceria Supported Catalysts for Steam Reforming of Methane. *ChemistrySelect*, 9(19), e202401393.
36. Turap, Y., Wang, I., Fu, T., Wu, Y., Wang, Y., Wang, W. (2020). Co–Ni alloy supported on $CeO_2$ as a bimetallic catalyst for dry reforming of methane. *International Journal of Hydrogen Energy,* 45(11), 6538-6548.
37. Liang, X., Wang, Q., Liu, S., An, S., Song, X. (2021). Shape control of exposed planes in ceria-zirconia based electrocatalysts for methanol oxidation. *International Journal of Hydrogen Energy*, 46(54), 27483-27494.
38. Moraes, T. S., Neto, R. C. R., Ribeiro, M. C., Mattos, L. V., Kourtelesis, M., Ladas, S., Noronha, F. B. (2016). Ethanol conversion at low temperature over $CeO_2$ Supported Ni-based catalysts. Effect of Pt addition to Ni catalyst. *Applied Catalysis B: Environmental*, 181, 754-768.
39. Araiza, D. G., Gómez-Cortés, A., Díaz, G. (2020). Effect of ceria morphology on the carbon deposition during steam reforming of ethanol over Ni/$CeO_2$ catalysts. *Catalysis Today*, 349, 235-243.
40. M. Kourtelesis, T. S. Moraes, L. V. Mattos, D. K. Niakolas, F. B. Noronha, X. Verykios, B 2021, *Appl. Catal.,* 2, 119.
41. Yang, S., Zhou, F., Liu, Y., Zhang, L., Chen, Y., Wang, H.,Liu, D. (2019).

Morphology effect of ceria on the performance of $CuO/CeO_2$ catalysts for hydrogen production by methanol steam reforming. *International Journal of Hydrogen Energy*, 44(14), 7252-7261.

42. Soykal, I. I., Bayram, B., Sohn, H., Gawade, P., Miller, J. T., Ozkan, U. S. (2012). Ethanol steam reforming over $Co/CeO_2$ catalysts: Investigation of the effect of ceria morphology. *Applied Catalysis A: General*, 449, 47-58.
43. LI, R. J., Zhang, J. P., Jian, S. H. I., LI, K. Z., LIU, H. L., Xing, Z. H. U. (2022). Regulation of metal-support interface of $Ni/CeO_2$ catalyst and the performance of low temperature chemical looping dry reforming of methane. *Journal of Fuel Chemistry and Technology*, 50(11), 1458-1470.
44. Wang, Y., Zhu, S., Lu, J., He, S., Lu, H., Song, D.,Luo, Y. (2023). Novel nanowire self-assembled hierarchical $CeO_2$ microspheres loaded with nickel-based catalysts for hydrogen production from steam reforming of glycerol. *Fuel Processing Technology*, 243, 107677.
45. Gao, S., Li, Y., Guo, W., Ding, X., Zheng, L., Wu, L., Wang, Y. (2022). Morphology effect of ceria support with hierarchical structure on the catalytic performance for nickel-based catalysts in dry reforming of methane. *Molecular Catalysis*, *533*, 112766.
46. Dong, C., Zhou, Y., Ta, N., Liu, W., Li, M., Shen, W. (2021). Shape impact of nanostructured ceria on the dispersion of Pd species. *Chinese Journal of Catalysis*, 42(12), 2234-2241.
47. Dragan, G., Kutarov, V., Schieferstein, E., Iorgov, A. (2021). Adsorption hysteresis in open slit-like micropores. *Molecules*, 26(16), 5074.
48. Vecchietti, J., Pérez-Bailac, P., Lustemberg, P. G., Fornero, E. L., Pascual, L., Bosco, M. V., Bonivardi, A. L. (2022). Shape-controlled pathways in the hydrogen production

from ethanol steam reforming over ceria nanoparticles. *ACS catalysis*, 12(16), 10482-10498.

49. D. Pashchenko, I. Makarov, Energy 2021, 222, 119993.
50. Zhang, Y., Zhao, S., Feng, J., Song, S., Shi, W., Wang, D., Zhang, H. (2021). Unraveling the physical chemistry and materials science of $CeO_2$-based nanostructures. *Chem*, 7(8), 2022-2059.
51. González-Castaño, M., Dorneanu, B., Arellano-García, H. (2021). *Reaction Chemistry & Engineering*, 6, 954
52. Konsolakis, M., Lykaki, M., Stefa, S., Carabineiro, S. A., Varvoutis, G., Papista, E., Marnellos, G. E. (2019). $CO_2$ hydrogenation over nanoceria-supported transition metal catalysts: Role of ceria morphology (nanorods versus nanocubes) and active phase nature (Co versus Cu). *Nanomaterials*, 9(12), 1739
53. Yao, S. Y., Xu, W. Q., Johnston-Peck, A. C., Zhao, F. Z., Liu, Z. Y., Luo, S., Rodriguez, J. A. (2014). Morphological effects of the nanostructured ceria support on the activity and stability of $CuO/CeO_2$ catalysts for the water-gas shift reaction. *Physical Chemistry Chemical Physics*, 16(32), 17183-17195.
54. Ren, Z., Peng, F., Li, J., Liang, X., Chen, B. (2017). Morphology-dependent properties of $Cu/CeO_2$ catalysts for the water-gas shift reaction. *Catalysts*, 7(2), 48.